Individual Component Map of Rotatory Strength and Rotatory Strength Density Plots As Analysis Tools of Circular Dichroism Spectra of Complex Systems

Le Chang,[†,#] Oscar Baseggio,[‡,#] Luca Sementa,[§] Daojian Cheng,[†] Giovanna Fronzoni,[‡] Daniele Toffoli,[‡] Edoardo Aprà,[‖] Mauro Stener,*[‡] and Alessandro Fortunelli*[§]

[†]Beijing Key Laboratory of Energy Environmental Catalysis, State Key Laboratory of Organic−Inorganic Composites, Beijing University of Chemical Technology, Beijing 100029, People's Republic of China

[‡]Dipartimento di Scienze Chimiche e Farmaceutiche, Università di Trieste, 34127 Trieste, Italy

[§]CNR-ICCOM & IPCF, Consiglio Nazionale delle Ricerche, via Giuseppe Moruzzi 1, 56124 Pisa, Italy

[‖]William R. Wiley Environmental Molecular Sciences Laboratory, Pacific Northwest National Laboratory, Richland, Washington 99352, United States

S *Supporting Information*

ABSTRACT: We introduce individual component maps of rotatory strength (ICM-RS) and rotatory strength density (RSD) plots as analysis tools of chiro-optical linear response spectra deriving from time-dependent density functional theory (TDDFT) simulations. ICM-RS and RSD allow one to visualize the origin of chiro-optical response in momentum or real space, including signed contributions and therefore highlighting cancellation terms that are ubiquitous in chirality phenomena, and should be especially useful in analyzing the spectra of complex systems. As test cases, we use ICM-RS and RSD to analyze circular dichroism spectra of selected (Ag−Au)$_{30}$(SR)$_{18}$ monolayer-protected metal nanoclusters, showing the potential of the proposed tools to derive insight and understanding, and eventually rational design, in chiro-optical studies of complex systems.
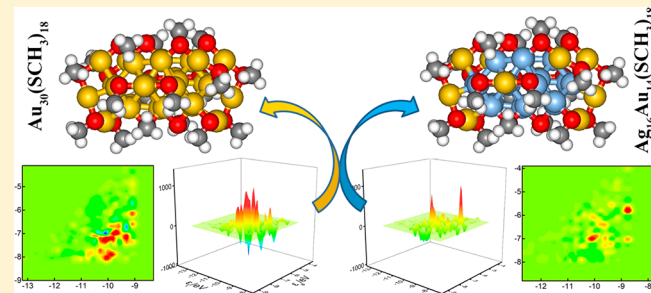
INTRODUCTION

Nanometer-scale, monolayer-protected metal clusters (MPCs) constitute a class of compounds of intrinsic fundamental interest and with momentum applications, e.g., in chiro-optoelectronics and biosensing, and have so attracted rapidly increasing attention over the past 20 years.[1−3] In particular, thiolate-protected gold nanoclusters with well-defined Au$_x$(SR)$_y$ stoichiometry and X-ray resolved crystal structure, sometimes called "gold nanomolecules",[4] combining features of gold nanoclusters and molecular compounds, have emerged as very interesting MPCs in both basic and applied studies, due to the possibility of achieving a high-level and thorough characterization of these systems using the rich palette of experimental and theoretical techniques available for stoichiometric and structurally resolved compounds.[2,5−7] However, despite the great interest raised and the considerable efforts devoted to the investigation of their properties, the origin of their distinct chiro-optical response still presents questions to be clarified and unresolved issues, therefore hindering a systematic rational design of optimal systems. A variety of interactions and an interplay of different physical phenomena (at the electronic level: preplasmonic features, many-body effects, resonances, conjugation, combined with structural

floppiness) in fact determine the chiro-optical landscape of gold nanomolecules.[8] On one hand, this makes these systems interesting as *realistic prototypes* of nanostructured metals and *in general of complex systems*. On the other hand, this hinders a facile interpretation of their response, in the same way as it occurs for less characterized metal nanoparticles. Analysis tools that allow one to model and master in a simplified way the origin and basic features of the chiro-optical properties of these and other complex (multicomponent) systems are strongly needed to advance rational design in this field.

In this perspective, theoretical approaches, such as time-dependent density functional theory (TDDFT), can play a fundamental role, due to the possibility of disentangling and dissecting, via in-depth analysis, the basic interactions in these complex, multicomponent, and multifunctional systems. TDDFT analysis tools proposed so far have more often focused on the analysis of absorption spectra,[9−11] while fewer efforts have been dedicated to circular dichroism (CD) spectra,[12−14] despite their importance in bio- and/or interfacial systems.[15] This is due to the difficulty in deriving structure/

1

property relationships in the chirality field. Chiro-optical activity is in fact intrinsically more complex than absorption.[16] First, chiro-optical activity has a *bisignate* nature (as opposed to the monosignate nature of absorption), often leading to cancellation between, e.g., response along different polarization axes (in experiment, the rotational average of the response is usually measured, not individual components). Second, the calculated optical rotation, especially at low energy, can be determined by the sum of very many (hundreds) off-resonance excitations,[16] not just a few dominant contributions, and this feature, as will be seen in the following, is exacerbated in complex systems. In the literature, one avenue has been to simplify the system's electronic structure by resorting to approximate but more readily interpretable approaches such as Hückel theory and to predict CD activity via an analysis of the corresponding matrix elements, with satisfactory success for the π-system of simple conjugated molecules.[16] More sophisticated approaches have derived the decomposition of optical rotation tensor in terms of localized molecular orbital (MO) contributions, such as bonds and lone pairs.[17,18] This real-space fragment analysis has allowed the rationalization of several difficult cases, such as the exceptionally large optical rotation of sterically hindered organic species (as in the example of norbornenone[17]). Other advanced approaches have focused on the decomposition of optical activity in terms of sum-overstates[19] or linear-response[20] formalisms and are closely related to the present proposal, from which they differ basically by limiting the analysis to few states or orbitals which—as we will see in the following—is somewhat restrictive in complex systems: in Section 2 we will discuss in more detail the comparison among our and these previous approaches.

To make progress in the direction of a deeper understanding and rational design of chiral phenomena, here we present and discuss two complementary tools to analyze chiro-optical linear response spectra derived from TDDFT simulations. One tool, which we name individual component map of rotatory strength (ICM-RS), follows the lines of and deepens the connection between response property and single-particle excitations in the density-matrix form of linear-response self-consistent theory[9,10,20] and allows one to visualize the main source of chiro-optical response in the space of occupied/virtual excitations, i.e., in momentum space. A second tool, rotatory strength density (RSD) plots, allows one to visualize the distribution of chiro-optical response in real space, thus lending itself to further (e.g., real-space fragment) analysis.[16−21] ICM-RS and RSD allow one to identify both the single-particle-excitation nature of the excited state and also to take into account the contribution of the dipole matrix elements (ICM-RS) or the atomic/molecular components (RSD) to the rotatory strength, with special emphasis on their *signs* (e.g., the relative signs of magnetic dipole vs electric-dipole-induced density-matrix elements in ICM-RS), therefore visualizing and immediately singling out cancellation terms due to interference between dipole and density-matrix components which are ubiquitous in chiro-optical response.[14,16−20]

As test cases of the proposed approach, we take selected $(Ag−Au)_{30}(SR)_{18}$ MPC monolayer-protected clusters, which exhibit a phenomenology that is rich and general enough to demonstrate the usefulness and potential of our approach in chiro-optical studies of complex systems.

The article is organized as follows. In Section 2 we describe the foundations of the approach and provide computational details. In Section 3 we present results of the ICM-RS and RSD analysis on the selected test systems and try to derive elements of general significance. Conclusions and perspectives are drawn in Section 4.

2. THEORETICAL APPROACH

DFT single-point and geometry relaxations were performed using the CP2K package[22] which is based on a hybrid Gaussian/Plane-Wave scheme (GPW).[23] Pseudopotentials derived by Goedecker, Teter, and Hutter (GTH)[24] were chosen to describe the core electrons and DZVP basis sets[25] to represent the DFT Kohn−Sham orbitals. The semiempirical Grimme-D3 correction[26] was added to the Perdew−Burke−Ernzerhof (PBE)[27] exchange and correlation (xc-) functional to take into account dispersion interactions. The cutoff for the auxiliary plane-wave representation of the density was 300 Ry.

As test cases to demonstrate the potentiality of the ICM-RS and RSD analysis we considered $(Ag−Au)_{30}(SR)_{18}$ MPC nanoclusters. In detail, we took the experimental X-ray-solved geometry of $Au_{30}(S^tBu)_{18}$[28] as a starting point, replaced the S^tBu ligands with SCH_3 for computational reasons, considered both pure $Au_{30}(SCH_3)_{18}$ and selected derivative $(Ag−Au)_{30}(SCH_3)_{18}$ compounds obtained by replacing some of the Au atoms with Ag atoms (see Section 3), and finally performed full geometry relaxations using the CP2K package to determine the equilibrium structures.

On the thus derived geometries, TDDFT simulations of both absorption and CD spectra were performed using the complex-polarizability TDDFT method implemented in the ADF package[29] and described in detail in previous articles,[30−33] to which we refer for more information and thorough comparison and validation with standard TDDFT approaches. The LB94[34] xc-functional was employed in the KS equations, while the exchange-correlation kernel in the TDDFT part is approximated according to the adiabatic local density approximation (ALDA).[35] A basis set of Slater type orbitals (STOs) included in the ADF database of triple-ζ polarized (TZP) quality was employed, which has proven to provide fully converged results.[32] The zero-order regular approximation (ZORA)[36] was employed to include relativistic effects, which are important for heavy elements such as gold.

As anticipated in the Introduction, in the present work we introduce two analysis tools to understand the nature of the chiro-optical peaks: the individual component maps of rotatory strength (ICM-RS) and rotatory strength density (RSD) plots.

The ICM-RS plots are obtained as follows. The z-component of the rotatory strength at each given frequency (energy) can be calculated as the imaginary part of the zz diagonal element of the circular dichroic tensor (the quantity denoted as $\beta_{zz}(\omega)$ in eqs 23 and 25 of ref 33)

$$CD_z(\omega) = -\frac{3\varepsilon}{2}Im\left(i \sum_i^{occ} \sum_a^{virt} \langle \varphi_i | m_z | \varphi_a \rangle \overline{\overline{P}}_i^a[\mu_z] \right)$$

$$= -\frac{3\varepsilon}{2}Im\left(i \sum_i^{occ} \sum_a^{virt} \langle \varphi_i | \mu_z | \varphi_a \rangle \overline{P}_i^a[m_z] \right) \quad (1)$$

where in the first equality of eq 1 ε corresponds to a Lorentzian energy broadening; $\overline{P}_i^a[\mu_z]$ is a density-matrix element due to the perturbation induced by the z-component of the electric dipole; and $\langle \varphi_i | m_z | \varphi_a \rangle$ is a matrix element of the magnetic dipole over a pair of occupied/virtual single-particle

2
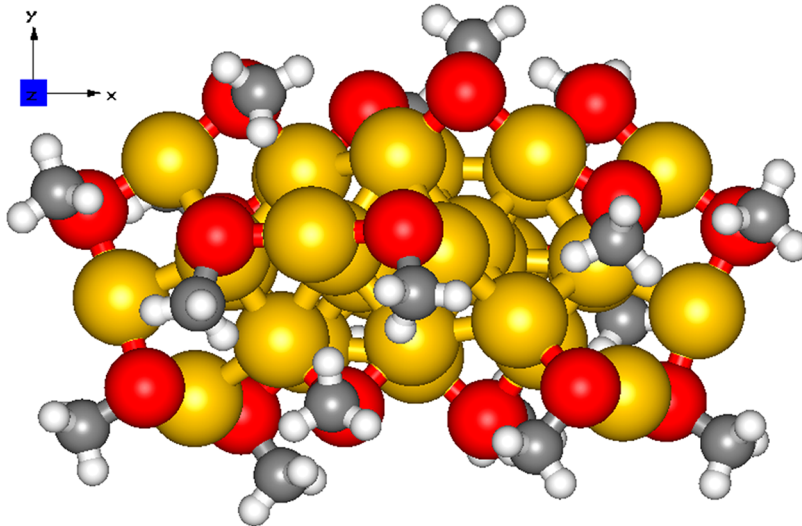
Figure 1. Pictorial illustration of the structure of the $Au_{30}(SCH_3)_{18}$ nanocluster. Au in yellow, S in red, C in gray, and H in white color. The axis system is also shown, with the z axis perpendicular to the plane of the figure.

molecular orbitals. $\overline{\overline{P}}_i{}^a[\mu_z]$ in our approach is obtained via eq 24 of ref 33, which we report here for sake of completeness:

$$\overline{\overline{P}}_i{}^a[\mu_z] = t_k(\omega)\left[\langle\varphi_a|\mu_z|\varphi_i\rangle + \sum_{\mu\tau}^{\text{fit}} (A^k)_{ia,\mu}^+ L_{\mu\tau} b_\tau\right] \tag{1a}$$

All the terms contained in eq 1a are defined and explained in ref 33. Completely analogous expressions hold for the x- and y-components of $CD(\omega)$. In the rightmost side of eq 1 an alternative, equivalent form of the rotatory strength $CD(\omega)$ is also reported, expressed in terms of density-matrix elements due to the perturbation induced by the z-component of the magnetic dipole, $\overline{P}_i{}^a[m_z]$, and matrix elements of the electric dipole $\langle\varphi_i|\mu_z|\varphi_a\rangle$, following eqs 25 and 26 of ref 33, which we report here for sake of completeness:

$$\overline{P}_i{}^a[m_z] = t_k(\omega)\langle\varphi_a|m_z|\varphi_i\rangle + s_k(\omega)\sum_{\mu\tau}^{\text{fit}} (A^k)_{ia,\mu}^+ L_{\mu\tau} g_\tau \tag{1b}$$

All the terms contained in eq 1b are defined and explained in ref 33. We report this alternative, equivalent expression for completeness and for future reference (see the analogous eqs 7 and 8 of ref 20), while using in practice in the present work exclusively the form given in terms of $\overline{\overline{P}}_i{}^a[\mu_z]$ and $\langle\varphi_i|m_z|\varphi_a\rangle$, which is repeated explicitly for the convenience of the reader in Section 3.1.

We pause here to discuss the dependence of eq 1 with respect to the choice of the gauge (orientation and origin of the reference system). ICM-RSs depend upon the orientation of the system since they are calculated along the three Cartesian x, y, z components. This dependence can be useful when the system displays some symmetry, in which case it will be possible to associate each dipole component with a well-defined irreducible representation of the excited state (assuming a totally symmetric ground state). When the system has no symmetry, the choice of axes is arbitrary, but the molecular orientation must be specified in order to exploit the information from the ICM-RS analysis and is here reported in Figure 1. Indeed, it should be recalled that many studies have shown that the isotropic average of optical rotation is small in

many systems because of the cancellation of Cartesian components with opposite signs and that a large isotropic value is often associated with a strong imbalance of positive and negative components. The dependence upon the choice of the origin of the refence system is more subtle. ICM-RS intrinsically exhibits the same behavior with the choice of the origin as the values of the rotatory strength (RS) obtained by TDDFT.[37] The RS is not origin-dependent when the electric dipole matrix elements are calculated in velocity gauge, but it is origin-dependent for other choices of the gauge, and the sensitivity with respect to this choice depends on the quality of the basis set. In the present work we employ the same basis set as in ref 33 in which thorough tests have shown that results obtained in the velocity gauge and the electric dipole gauge are in excellent agreement, confirming the good quality of the chosen basis set and therefore the independence of the results with respect to the origin.

ICM-RSs can be plotted either in 2D as contours or in 3D in full scale and are plotted as a function of the energies of the molecular orbitals corresponding to the i and a indexes of eq 1, while the Z-axis in the 3D plots corresponds to the ICM-RS values. In the ICM-RS plots reported in Section 3, a color scale is used to visualize different values of the $\langle\varphi_i|m_z|\varphi_a\rangle\overline{\overline{P}}_i{}^a[\mu_z]$ products. We finally note that each $\langle\varphi_i|m_z|\varphi_a\rangle\overline{\overline{P}}_i{}^a[\mu_z]$ product, corresponding to a point in the XY plane, is smoothed by broadening with a Gaussian function with fwhm = 0.12 eV, thus turning a set of delta-like points into a smooth surface. The width of the Gaussian is a purely empirical parameter, which we choose on the basis of graphical convenience. For a precise identification, we use the notation ICM-RS(ω, x or y or z): "x or y or z" denotes the Cartesian components of the polarization axis, while ω is the excitation frequency (or alternatively, the energy).

It should be noted that in a previous proposal, named transition component mapping (TCM),[10] the square of $\overline{\overline{P}}_i{}^a[\mu_z]$ quantities as a function of the one-electron or single-particle energies ε_i and ε_a were plotted, with individual contributions smeared by a Gaussian function to make them visually clearer as we do here. However, TCM is more focused on a description of the excited state than being suited to rationalize

3

the mechanisms which are behind absorption or circular dichroism spectra. In fact in TCM (i) the contribution of the matrix elements of the dipole to the absorption or rotatory strength intensity and thus also (ii) the relative sign of dipole and induced-density-matrix elements of the individual single-particle excitations are lost. In other words, the information on the *coherence or interference* between the distortion in the system's wave function due to the external perturbation and the value of the property is lost. These drawbacks are overcome in ICM-RS by deriving appropriate formulas for rotatory strength in eq 1 and by plotting not simply the square of density-matrix elements but rather the products $\langle \varphi_i |$ $m_z | \varphi_a \rangle \overline{\overline{P}}_i^a [\mu_z]$, i.e., the full individual single-particle contributions as functions of the one-electron or single-particle energies ε_i and ε_a: thus, the proposed name of individual component maps of rotatory strength (ICM-RS). The resulting plots are suited for analyzing chiro-optical response and, by including both density-matrix and dipole contributions, allow one to single out and quantitatively assess within this response its positive and negative components, which lead to enhancement or damping of rotatory strength, respectively. It must be stressed that the total rotatory strength intensity at each given energy or frequency ω is proportional to the *integral* of the ICM-RS(ω, x or y or z) over the ($\varepsilon_i, \varepsilon_a$) plane, so that negative and positive contributions destructively interfere and cancel each other. Indeed, the rotatory strength, CD(ω), is from a mathematical point of view the scalar product, i.e., the integral over the ($\varepsilon_i, \varepsilon_a$) plane, of density-matrix, and magnetic dipole operators. Useful plots complementary to ICM-RS are thus plots in the ($\varepsilon_i, \varepsilon_a$) plane of the contribution of the individual components of the electric dipole (ED) and magnetic dipole (MD) operators, i.e., ICM-ED$[\mu_{x,y,z}]$ and ICM-MD$[m_{x,y,z}]$ plots, respectively, which will be reported in the SI for the reader's convenience.

In the literature, formulas for the rotatory strength lending themselves to analyses alternative to eq 1 have been derived. In particular, in ref 17 optical rotation has been given in terms of a sum over occupied orbitals of matrix elements involving derivatives of such orbitals with respect to perturbing electric and magnetic fields, thus leading—after a transformation conveniently producing localized occupied orbitals—to a decomposition of optical rotation in terms of bond and lone-pair components. This formulation can be seen as being related to eq 1 by summing over virtual orbitals. This real-space analysis has allowed the rationalization of several difficult cases, such as the exceptionally large optical rotation of norbornenone in ref 17. The merit of this approach is a direct representation of optical rotation in real space and in terms of localized molecular orbitals which are ultimately connected with molecular fragments. The drawback is that some information is lost in this approach, e.g., when excitations coupling the same occupied orbitals with different virtual orbitals are important in determining CD spectra as will be specifically found in one of the examples investigated below. Another approach based on a sum-overstates analysis has been proposed in ref 19 and has later been complemented by a linear-response analysis[20] that is closely related to the present proposal. Our eq 1 is in fact equivalent to eqs 6, 7, and 8 of ref 20 (with the difference that we keep the 3 Cartesian components separated), and—analogously to the present ICM-RS proposal—plots of individual contributions have also been utilized as graphical analysis tools of TDDFT

simulations (see, e.g., Figure 1 of ref 20). Our approach differs from this previous proposal because in ICM-RS plots we use the pristine (ε_i, ε_a) plane, and we do not attempt to order contributions in terms of their weight with the final aim of reducing optical rotation to only a few states or orbital contributions. We find in fact that this is restrictive in complex systems such as MPC and may lead us to miss important information, such as the competition between different regions of the (ε_i, ε_a) plane discussed at length in Section 3: this is already crucial in small MPC species such as those investigated here and should become even more extreme when the number of excitations contributing to the response diverges, e.g., in the case that a plasmonic collective behavior arises. As a crucial point, it should be recalled that a sum-overstates analysis has shown that—despite its unusual features—the optical rotation of norbornenone is in fact dominated by only the first term in the sum (its first excited state),[19] a simplification which is reasonable in small molecules but does not hold in complex systems such as MPC,[38] as we will specifically see in the following.

We also note that, while ICM-RS analysis deals with chiro-optical response, a parallel analysis can be analogously conducted for optical absorption (the other component of linear response), as done in previous work,[38] in which we have introduced individual component maps of oscillatory strength (ICM-OS) plots and employed them to analyze and rationalize optical absorption spectra of $(Ag-Au)_{36}(SPh)_{24}$ nanomolecules. ICM-OS plots for the investigated systems will also be reported in Section 3 for completeness. We have also explored the possibility of combining ICM-OS and ICM-RS plots to visualize the *ratio* of CD and absorption, which provides a different normalization of chiro-optical response potentially useful in some cases. This possibility is not reported here as it did not produce particularly illuminating results in the present context but will be considered in future work.

The second analysis tool we introduce in the present work to understand the nature of the chiro-optical peaks is the rotatory strength density (RSD) plot. To this aim, we use an alternative expression for the z-component of the rotatory strength at each given frequency (energy), i.e.

$$CD_z(\omega) = -\frac{3\varepsilon}{2} Re\left(\int d\overline{r} \cdot z \cdot \rho_{m_z}^{(1)}(\omega, \overline{r}) \right)$$
$$= -\frac{3\varepsilon}{2} Re\left(\int_{\overline{r}'=\overline{r}} d\overline{r} \cdot \hat{m}_z(\overline{r}) \rho_{\mu_z}^{(1)}(\omega, \overline{r}, \overline{r}') \right) \quad (2)$$

where in the first equality of eq 2 the product of the induced density due to the magnetic dipole perturbation, $\rho_{m_z}^{(1)}(\omega, \overline{r})$, times the electric dipole is integrated over the space to give the CD. As in the case of eq 1, expressions completely analogous to eq 2 hold for the x- and y-components of CD(ω). This definition lends itself to an immediate visualization in real space by plotting the $Re(z \cdot \rho_{m_z}^{(1)}(\omega, \overline{r}))$ quantity as, e.g., 3D contours: we name such plots as RSD plots. For a precise identification, we use the notation RSD(ω, x or y or z): "x or y or z" denotes the Cartesian components of the polarization axis, while ω is the excitation frequency (or alternatively, the energy).

In the rightmost side of eq 2 we also provide an alternative expression of CD(ω) in terms of the electric dipole perturbation. At variance with eq 1 which can be straightforwardly used in both equivalent symmetric formulations to produce ICM-RS plots, this alternative CD definition

4
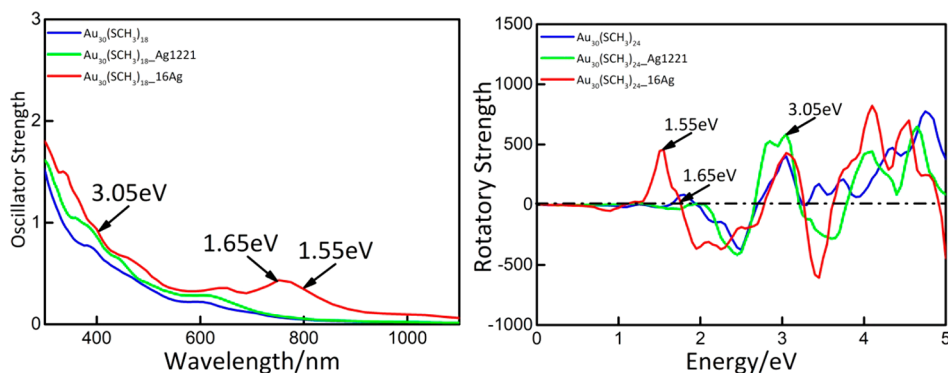
Figure 2. Optical absorption (left) and circular dichroism, CD (right), spectra of $Au_{30}(SR)_{18}$, $Ag_2Au_{28}(SR)_{18}$, and $Ag_{16}Au_{14}(SR)_{18}$ nanoclusters as predicted by our DFT/TDDFT approach. Oscillator strengths and rotatory strengths are reported for absorption and CD, respectively.

is less convenient to be employed in practice since the magnetic dipole operator is not a simple multiplicative operator, at variance with the electric dipole. In eq 2 we in fact introduce a generalized density matrix, in which, following eq 5.2.5 of ref 9, $\overline{r}' = \overline{r}$ is set *after* the operator has acted on the density but *before* integration. We report this alternative expression for completeness and for future reference, while using in practice in the present work exclusively in the form given in terms of $\rho_{m_z}^{(1)}(\omega,\overline{r})$, which is repeated explicitly for the convenience of the reader in Section 3.1.

Note that we try to present formulas as general as possible because one of the goals of the present work is to introduce a comprehensive setup that can be used to study systems for which alternative formulations or quantities may be more useful and informative than for the systems here investigated.

3. RESULTS AND DISCUSSION

The MPC system we choose as a test case of our analysis is $Au_{30}(SR)_{18}$ and selected Ag-alloyed derivatives. $Au_{30}(SR)_{18}$ MPC compound has been synthesized experimentally; its crystal structure has been solved; and it has been subjected to extensive experimental and theoretical investigations (see refs 21, 28, 39, 40, and references therein). Figure 1 reports a pictorial illustration of the framework structure of $Au_{30}(SR)_{18}$ nanoclusters, R = CH_3, while Figure 2 reports the optical absorption and circular dichroism (CD) spectra of the (Ag–Au)$_{30}(SR)_{18}$ nanoclusters here investigated as predicted by our DFT/TDDFT approach (see Section 2 for computational details). Note that, here and in the following, we use the common practice of reporting absorption spectra as a function of wavelength (measured in nm) and CD spectra as a function of excitation energy (given in eV): the conversion between the two energy units is immediate and should not give rise to ambiguity.

The framework structure of $Au_{30}(SR)_{18}$ does not exhibit any symmetry plane and is therefore intrinsically chiral, but an (approximate) C2 axis of symmetry is present, so that Au atoms are equivalent in pairs (for convenience of the reader, only symmetry-nonequivalent atoms are depicted and numbered in Figure S1 of the SI). It should be added that the structure of $Au_{30}(SR)_{18}$ is not only chiral but also belongs to the class of anisotropic MPC discussed in ref 41; i.e., it presents a significantly different response along the three Cartesian directions (see, e.g., ref 16 for a previous discussion of non-MPC systems). We therefore report CD spectra distinguished into Cartesian components of the polarization

axis in Figure S2 of the Supporting Information (SI), and in the following we focus on selected Cartesian components of each systems.

As apparent from Figure 2b, the rotatory strength of $Au_{30}(SR)_{18}$ is significant, but only above 2 eV (up to 600 nm). In order to have, for the sake of our analysis, a wider range of excitation energies and a wider set of test cases with a comparison among different but closely related systems, we chose to consider derivatives of $Au_{30}(SR)_{18}$ obtained via alloying with Ag, i.e., (Ag–Au)$_{30}(SR)_{18}$ nanoclusters. Mixed Ag–Au MPCs have been intensively studied in the literature in terms of UV–vis absorption spectra[42–45] (although (Ag–Au)$_{30}(SR)_{18}$ mixed systems have not yet been experimentally synthesized), and here we extend this line of studies to explore the effect of alloying on CD spectra.[46] As we will see in the following, the chiro-optical properties of the mixed (Ag–Au)$_{30}(SR)_{18}$ MPC are interesting and present an enhanced chiro-optical response, which make these systems appealing in terms of both fundamental studies and applications.

To select which (Ag–Au)$_{30}(SR)_{18}$ compositions and structures to investigate among the many possible ones, we performed a preliminary energy analysis. In detail, the energetics of single Ag doping into $Au_{30}(SR)_{18}$ according to our DFT approach (all structures DFT-optimized as described in Section 2) is reported in Table S1 and Figure S1 of the SI and show that the cluster sites can be partitioned into 5 groups as follows: (i) two sites in which Ag doping is optimally favorable (associated with the nonequivalent [12] site in Table S1 and Figure S1 of the SI), (ii) a set of 14 sites in which doping is less favorable by 5–8 k_BT at room temperature (the [4,6,8,10,13,14,15] sites in Table S1 and Figure S1), (iii) another two sites higher in energy at 9.5 k_BT (the [7] site), (iv) a set of 10 sites (including most staple sites) still higher in energy at 12–14 k_BT (the [1,2,3,5,9] sites), and finally (v) two (staple) sites energetically most unfavorable at 19 k_BT (the [11] site). Since energy differences of the first two groups of sites (i,ii) are a few times the thermal energy at room temperature, it is possible that in a real experiment a mixture of the energetically most stable and the second most stable sites will be produced (unless the system is equilibrated for a long time). We thus expect that the two lowest-energy sites (i) and possibly the next 14 doping sites (ii) will be appreciably populated under standard conditions, and we thus select three compounds for our analysis: $Au_{30}(SR)_{18}$, $Ag_2Au_{28}(SR)_{18}$, and $Ag_{16}Au_{14}(SR)_{18}$ nanoclusters, where $Ag_2Au_{28}(SR)_{18}$ and $Ag_{16}Au_{14}(SR)_{18}$ are obtained by replacing Au with Ag in the two most stable doping sites of $Au_{30}(SR)_{18}$ [$Ag_2Au_{28}(SR)_{18}$] or
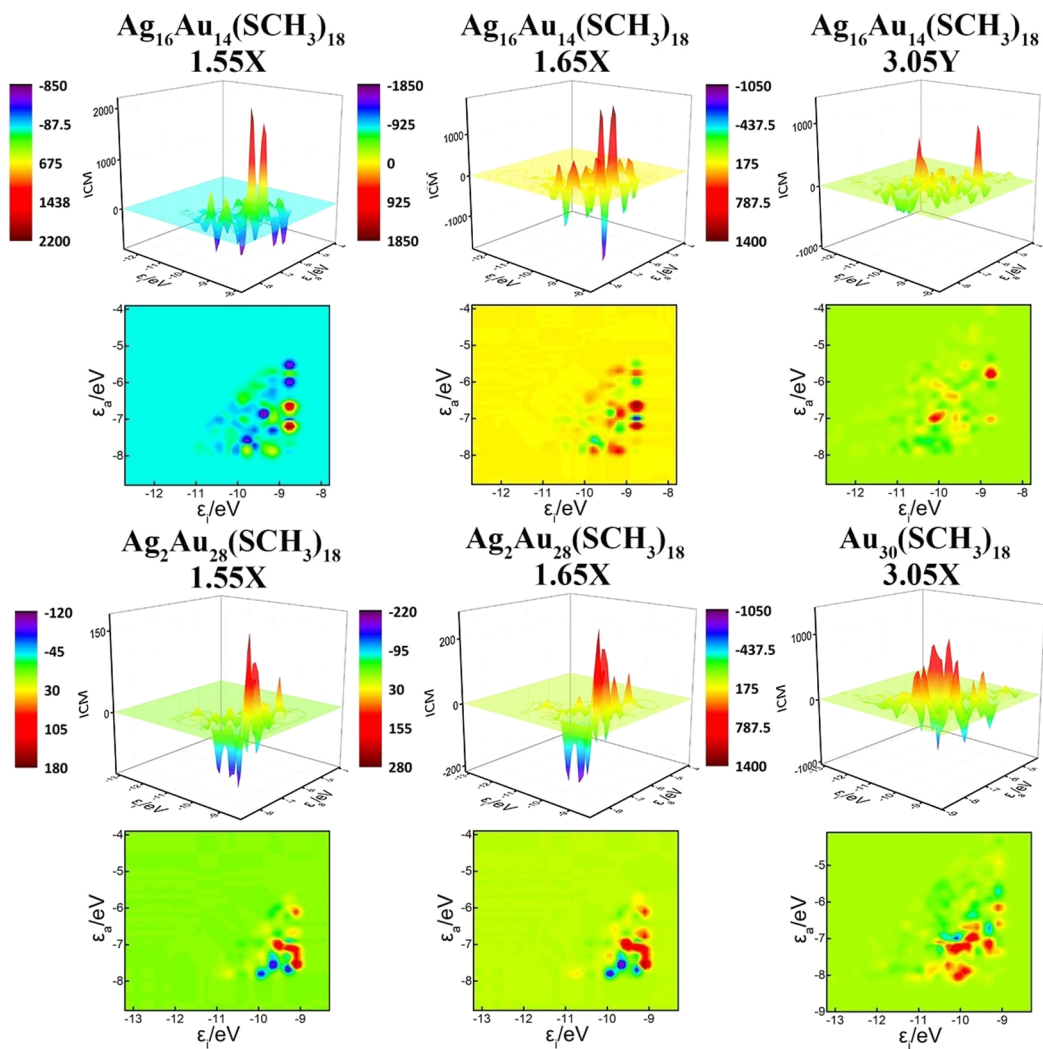
Figure 3. 2D (contour, upper panels of each given system and excitation energy) and 3D (full scale, lower panels of each given system and excitation energy) ICM-RS(ω, x or y or z) plots along various polarization axes (as indicated) and at 3 different excitation energies (1.55 eV, left, 1.65 eV, middle, and 3.05 eV, right) for the $Au_{30}(SR)_{18}$, $Ag_2Au_{28}(SR)_{18}$, and $Ag_{16}Au_{14}(SR)_{18}$ nanoclusters derived from our TDDFT calculations.

in the 16 most stable doping sites of $Au_{30}(SR)_{18}$ [$Ag_{16}Au_{14}(SR)_{18}$].

For the thus selected compounds, $Au_{30}(SCH_3)_{18}$, $Ag_2Au_{28}(SCH_3)_{18}$, and $Ag_{16}Au_{14}(SCH_3)_{18}$, optical absorption and CD spectra were simulated and are reported in Figure 2. The $Au_{30}(SR)_{18}$ nanocluster has been named "green gold" because it exhibits an absorption peak around 600 nm, which gives it a characteristic green color and is well reproduced by our TDDFT approach (see also Figure 2a in ref 28 and the related discussion). Doping with 2 and especially with 16 Ag atoms leads to a strong enhancement of absorption intensity in the low-energy optical region, with a well-defined peak developing at around 1.59 eV (780 nm) for $Ag_{16}Au_{14}(SCH_3)_{18}$. In parallel, the rotatory strength of the $Au_{30}(SR)_{18}$ nanocluster, which exhibits strong peaks at 2.58 and 3.02 eV (480 and 410 nm, respectively), is also enhanced and shifted at lower energies by Ag doping, so that $Ag_{16}Au_{14}(SCH_3)_{18}$ finally exhibits a CD spectrum with intense broad CD peaks all across the optical region: at 2.50−2.85, 1.95−2.25, and 1.55 eV (435−495, 550−640, and 800 nm, respectively). (Ag−Au)$_{30}(SR)_{18}$ MPC therefore presents a rich and interesting phenomenology in both the high- and low-energy optical region which lends itself to and actually asks for a deeper

analysis and understanding. These systems are therefore suitable as test cases of our approach.

3.1. ICM-RS and RSD Plots. We start with an ICM-RS analysis of the chiro-optical spectrum of $Au_{30}(SCH_3)_{18}$, $Ag_2Au_{28}(SCH_3)_{18}$, and $Ag_{16}Au_{14}(SCH_3)_{18}$ MPC. As discussed in Section 2, to obtain ICM-RS plots we use the definition of the rotatory strength, CD(ω), based on the product of electric-dipole-induced density-matrix and matrix elements of the magnetic dipole:

$$CD_z(\omega) = -\frac{3\varepsilon}{2} Re\left(\sum_i^{occ} \sum_a^{virt} \langle \phi_i | m_z | \phi_a \rangle \overline{\overline{P}}_i^a[\mu_z] \right)$$ (3)

where, as introduced in Section 2, $\overline{\overline{P}}_i^a[\mu_z]$ is a density-matrix element due to the perturbation induced by the z-component of the electric dipole, and $\langle \varphi_i | m_z | \varphi_a \rangle$ is a matrix element of the magnetic dipole over a pair of occupied/virtual single-particle molecular orbitals.

In Figure 3 we report 3-dimensional (3D) and 2-dimensional (2D) ICM-RS(ω, x or y or z) plots obtained from CD spectra predicted at 1.55, 1.65, and 3.05 eV for the (Ag−Au)$_{30}(SR)_{18}$ clusters here investigated and selected Cartesian components. We have chosen the data to be reported so as to
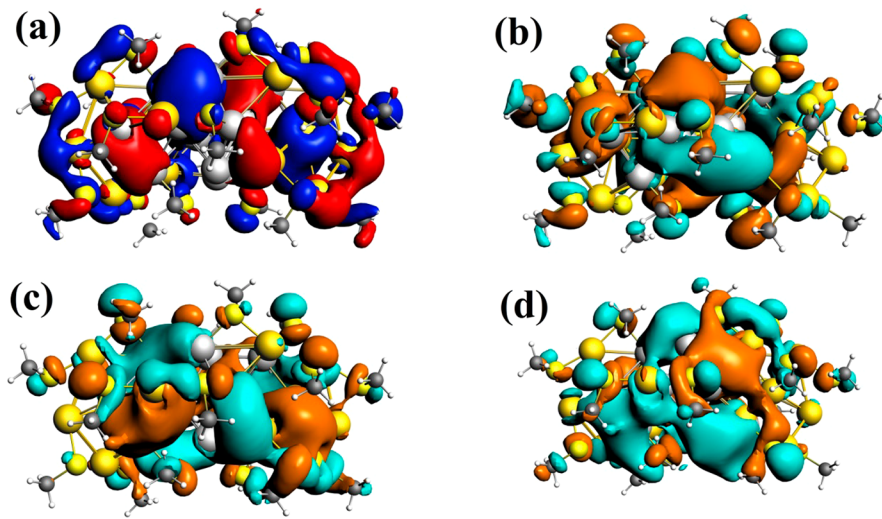
Figure 4. 3D contour plots of molecular orbitals of the $Ag_{16}Au_{14}(SR)_{18}$ nanoclusters most involved in the CD response at 1.55−1.65 eV as derived from our DFT calculations: (a) occupied orbital with energy of −8.76 eV; (b) virtual orbital with energy of −7.28 eV; (c) virtual orbital with energy of −7.00 eV; and (d) virtual orbital with energy of −6.80 eV. The isosurface values are 0.01 bohr$^{-3/2}$.
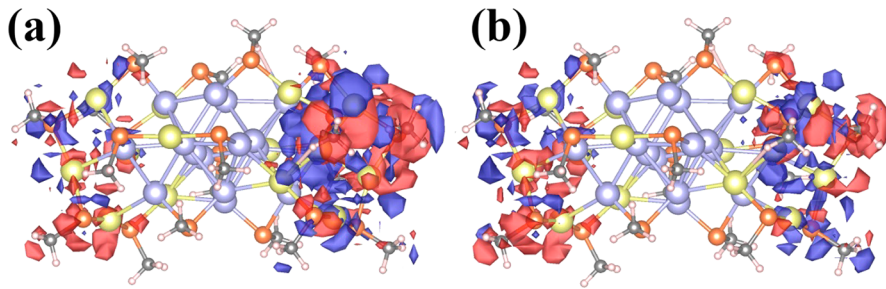
Figure 5. $RSD(\omega, x)$ plots along the x-axis of polarization for the $Ag_{16}Au_{14}(SR)_{18}$ nanocluster at two different excitation energies: (a) 1.55 eV, left, and (b) 1.65 eV, right, as derived from our TDDFT calculations. The contour values are the same in both panels and are equal to 7 electron/bohr.^{3}

single out the most interesting and representative cases: not all Cartesian components of the polarization axis are reported, but only those components whose contribution is dominant/representative of the overall chiro-optical response and physical behavior of the investigated systems (complete ICM-RS(ω, x or y or z) plots can be found in Figure S3 of the SI).

From an inspection of Figures 2b, 3, and S2 several observations are apparent.

First, at 1.55 eV $Au_{30}(SR)_{18}$ exhibits a weak CD rotatory strength because its chiro-optical activity is only incipient at this energy, and additionally, there is a compensation between x- and y-components of the polarization axis. In contrast, for $Ag_{16}Au_{14}(SR)_{18}$ the x-component of the polarization axis is clearly dominant (although also in this system there is some compensation between the x-component on one side and the z- and y-components on the opposite side). Analyzing the x-component of $Ag_{16}Au_{14}(SR)_{18}$ in detail, its ICM-RS plot in Figure 3 shows two major peaks (the red positive peaks towering the 3D plot) which correspond to single-particle excitations involving an occupied orbital with orbital energy of −8.76 eV and two virtual orbitals with orbital energies of −6.80 eV and −7.28 eV, respectively. To visualize these excitations in real space, Figure 4 shows contour plots of the involved occupied and virtual orbitals.

Second, it is interesting to note that, even at 1.55 eV at which the x-component of $Ag_{16}Au_{14}(SR)_{18}$ exhibits a

maximum in rotatory strength, there are significant negative contributions in the x-component ICM-RS plots, in particular contributions essentially corresponding to the off-diagonal upper part of the $(\varepsilon_i, \varepsilon_a)$ plane. Such contributions extend over a significant portion of this plane, in tune with previous observations that the calculated optical rotation is often determined by the sum of hundreds of single-particle excitation contributions[16] and realizes a progress in understanding by qualifying (signs) and quantifying (values) *which* regions of the $(\varepsilon_i, \varepsilon_a)$ plane contribute to the overall response (see also the discussion below).

To confirm this cancellation phenomenon, we resort to an RSD analysis. As discussed in Section 2, to obtain RSD plots we use the definition of the rotatory strength $CD(\omega)$ based on the product of the induced density due to the magnetic dipole perturbation, $\rho_{m_z}^{(1)}(\omega,\bar{r})$, times the electric dipole

$$CD_z(\omega) = -\frac{3\varepsilon}{2}\text{Re}\left(\int d\bar{r} \cdot z \cdot \rho_{m_z}^{(1)}(\omega,\,\bar{r})\right) \qquad (4)$$

and we plot the $z \cdot \rho_{m_z}^{(1)}(\omega,\bar{r})$ quantity as 3D contours in Figure 5.

The presence of significant negative contributions to CD is fully confirmed by this RSD plot: the x-axis RSD plot of $Ag_{16}Au_{14}(SR)_{18}$ at 1.55 eV shown in Figure 5a presents a clear alternation of positive and negative regions in real space, entailing strong cancellation effects.

7
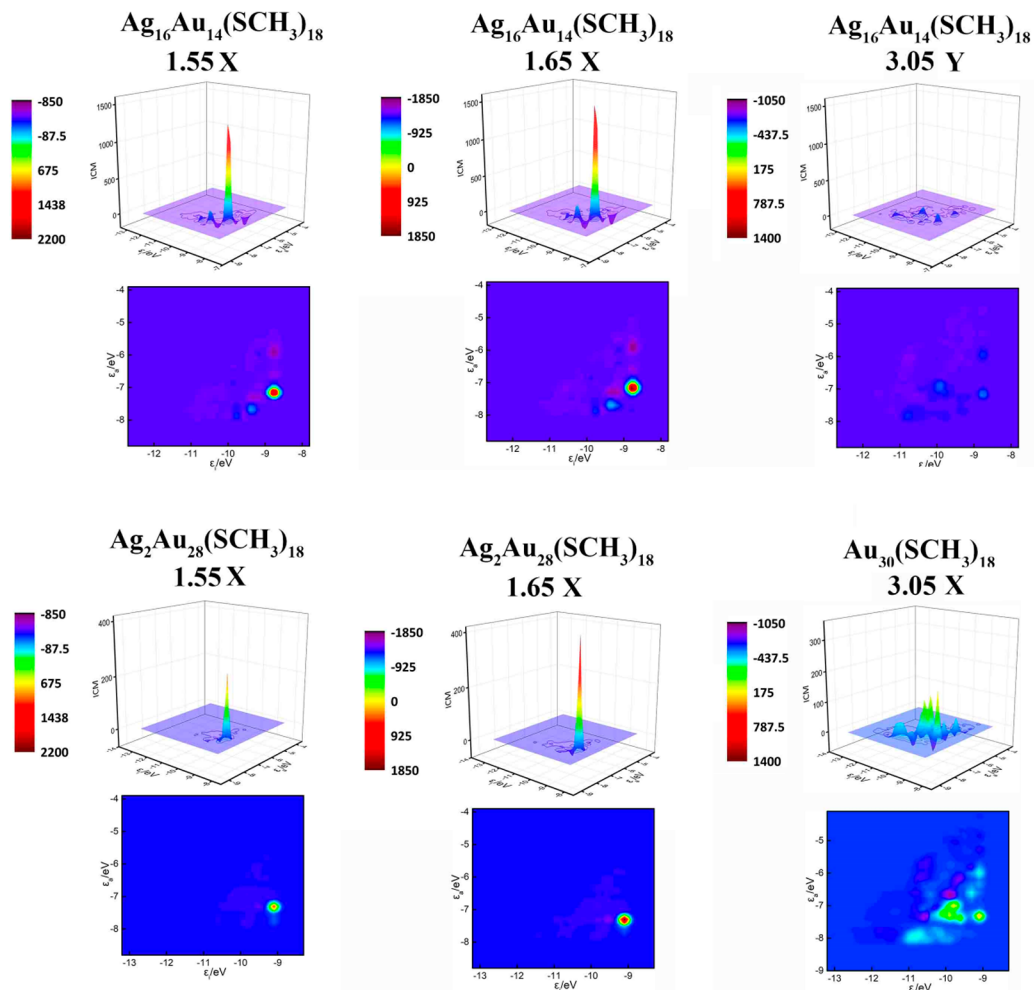
Figure 6. 2D (contour, upper panels) and 3D (full scale, lower panels) ICM-OS plots along various Cartesian axes of the electric field (as indicated) and at three different excitation energies (1.55 eV, left, 1.65 eV, middle, and 3.05 eV, right) for the $Au_{30}(SR)_{18}$, $Ag_2Au_{28}(SR)_{18}$, and $Ag_{16}Au_{14}(SR)_{18}$ nanoclusters derived from our TDDFT calculations.

In general, for $Ag_{16}Au_{14}(SR)_{18}$ we find that such cancellation effects are important for dichroism, whereas they are less important in absorption (as apparent from an inspection of Figure 6 where we report selected ICM-OS plots—note that this finding is not general, and strong destructive interference effects can occur also in absorption spectra[38,47]). Indeed in the systems here considered we find that absorption and dichroism have a significantly different behavior, as already suggested, e.g., by the mismatch between the maximum in absorption ($\approx$770 nm = 1.61 eV) and the maximum in CD ($\approx$800 nm = 1.55 eV) for $Ag_{16}Au_{14}(SR)_{18}$. For a more detailed comparison and for the sake of completeness we report in Figure 6 selected ICM-OS(ω) plots for the same systems here investigated corresponding to the ICM-RS(ω) plots of Figure 3.

Such a difference between absorption and dichroism becomes a divergence for $Ag_{16}Au_{14}(SR)_{18}$ at 1.65 eV (750 nm), at which energy absorption is only slightly below its peak height at 1.61 eV, whereas the rotatory strength goes through zero, both as average value and as x-component. It is then instructive to compare in Figure 3 the x-component ICM-RS plots of $Ag_{16}Au_{14}(SR)_{18}$ at 1.55 and 1.65 eV (i.e., ICM-RS(ω, x) plots at the energy of the maximum and the zero in CD, respectively). An inspection of the top-left and top-middle panels of Figure 3 shows that the zeroing in CD at 1.65 eV is caused by the insurgence of a strong negative peak which

corresponds to a single-particle excitation from an occupied orbital with orbital energy of −8.76 eV (the same involved in the two major positive ICM-RS peaks) to a virtual orbital with orbital energy of −7.00 eV. Notably, the contribution of this single-particle excitation to CD is basically negligible at 1.55 eV, but it rapidly increases up to destroying the contribution of the two other major excitations in one tenth of an eV. From an inspection of the involved molecular orbitals in Figure 4 it can be appreciated that the virtual orbital with energy of −7.00 eV has a different spatial arrangement with respect to the virtual orbitals with energy of −7.28 eV and −6.80 eV, which entails an opposite "skewness" of the orbital wave function in real space. This implies that the contribution of the (ε_i = −8.76 eV → ε_a = −7.00 eV) excitation to CD opposes the contribution of the (ε_i = −8.76 eV → ε_a = −7.28 eV; ε_a = −6.80 eV) excitations and, strongly increasing from 1.55 to 1.65 eV, eventually cancels them, thus rationalizing the fast decay of CD response.

The present analysis and the derived importance of cancellation effects coming from excitations localized in the same region of space suggest that the RSD analysis is less informative than the ICM-RS one in the present case. Indeed the comparison between RSD plots at 1.55 and 1.65 eV shown in Figure 5 is useful as it confirms significant cancellation effects in both cases and also suggests why there is a strong

decrease in the rotatory strength from 1.55 to 1.65 eV: note the significantly reduced values of the RSD taken at the same contour value from 1.55 to 1.65 eV. However, it is not easy to translate in an immediate way what can be visually captured from Figure 5 into a quantitative analysis of the evolution of the CD response, whereas this is possible using ICM-RS plots.

An ICM-RS analysis of $Ag_2Au_{28}(SR)_{18}$ between 1.55 and 1.65 eV presents a yet different scenario. Focusing on the x-component, it can be seen that the rotatory strength of $Ag_2Au_{28}(SR)_{18}$ is weaker than that of $Ag_{16}Au_{14}(SR)_{18}$ not only because the intensity of the ICM-RS(ω, x) peaks is smaller (attention should be paid to the different color scale of the ICM-RS plots for the two MPC compounds) but also as a result of a cancellation between contributions coming symmetrically from the upper-right (positive) and lower-left (negative) region of the ICM-RS plot. In other words, contributions coming from deep-HOMO-n → LUMO interfere destructively with contributions coming from HOMO → high-LUMO+m.

Passing now to the high-energy optical region, at 3.05 eV the ICM-RS plot along the x-polarization axis for the $Ag_{16}Au_{14}(SR)_{18}$ cluster (not shown) is qualitatively similar to that at 1.65 eV with strong peaks canceling each other, but a dichroic response along the y-axis has meanwhile significantly developed and has become the largest component in the CD spectrum. Analyzing in detail this new feature, one finds that the y-axis ICM-RS(ω, y) in Figure 3 is dominated by two major peaks, corresponding to excitations along the diagonal of the $(\varepsilon_i, \varepsilon_a)$ plane. These excitations are also present at 1.55 eV, where they are in phase and give a negative contribution, whereas they are still in phase but now both positive and, being the only major peaks surviving at this energy, produce a maximum also in the total (average) rotatory strength. Despite the ICM-RS plots now look more simplified, it can still be noted that negative contributions from long-range and off-diagonal excitations are spread over the $(\varepsilon_i, \varepsilon_a)$ plane and damp the CD response.

Finally, an analysis of the ICM-RS plots for low-doping $Ag_2Au_{28}(SR)_{18}$ and $Au_{30}(SR)_{18}$ systems at 3.05 eV shows that these plots are drastically different with respect to the plots at low energy. Focusing on the x-component of $Au_{30}(SR)_{18}$, which is the most intense, one finds a strong contribution of the lower-diagonal regions of the $(\varepsilon_i, \varepsilon_a)$ plane with some cancellation with the upper-diagonal region. This is thus drastically different with respect to the cancellation between upper-right and lower-left regions at 1.65 eV and, in some sense, is more similar to the ICM-RS plot of the $Ag_{16}Au_{14}(SR)_{18}$ system at 3.05 eV. Indeed, the lower-diagonal peaks of $Au_{30}(SR)_{18}$ are more intense than the upper-diagonal ones and build up a maximum in rotatory strength of height comparable to that of $Ag_{16}Au_{14}(SR)_{18}$.

To summarize the previous observations, we propose three different scenarios for the CD response and its possible damping due to cancellation effects, i.e.: (i) specific major peaks associated with excitations from a given occupied orbital to different virtual orbitals; (ii) off-diagonal upper vs lower regions of the $(\varepsilon_i, \varepsilon_a)$ plane in the ICM-RS plot; (iii) upper-right vs lower-left regions of the $(\varepsilon_i, \varepsilon_a)$ plane in the ICM-RS plot. These scenarios may be of general significance and provisionaly set the stage for a systematic analysis of MPC chiro-optical spectra to be conducted in future work.

It is worth noting that the physics behind the first two scenarios (i,ii) and the third scenario (iii) just outlined is different. The cancellation due to interference between specific peaks or upper/lower off-diagonal terms is in fact an outcome of a coupling between configurations with different orbital energy difference $\delta\varepsilon$ (with $\delta\varepsilon = \varepsilon_a - \varepsilon_i$), e.g., from the same given occupied orbital with energy ε_i to—say—two virtual orbitals with different energies ε_a and ε_a' and, therefore, different orbital energy difference $\delta\varepsilon = \varepsilon_a - \varepsilon_i$ and $\delta\varepsilon' = \varepsilon_a' - \varepsilon_i$. We expect this type of cancellation to be very sensitive to the details of the Hamiltonian coupling between the configurations and therefore in principle to be tunable by doping or changing the nature of the ligand, such as can be achieved, e.g., switching from thiolates to selenolates.[47] These first two scenarios therefore offer wide room and opportunities to tune the chiro-optical properties of the systems by rational design (as indeed found by considering the effects of doping in the present work). On the opposite, a cancellation due to interference between the upper-right and lower-left off-diagonal terms occurs among configurations with similar orbital energy difference, and this type of mixing may be expected to survive even after the system is perturbatively changed by doping or by changing the nature of the ligands, so that in this case it will be more difficult to tune the chiro-optical properties of the systems by a proper design of the cluster.

Before turning to conclusions, it is useful to underline once more an important point derived from the previous analysis, i.e., that typically, over the entire optical region from low to high energies, both absorption and CD spectra of the MPC systems here investigated are not determined by a single, dominant peak, but rather the chiro-optical response is spread over a significant domain of the $(\varepsilon_i, \varepsilon_a)$ plane, including long-range off-diagonal tails.[16] While deferring a systematic study of MPC and other metal nanoclusters to future work, we anticipate that this seems to represent a general feature of the absorption and particularly the CD spectra of *complex systems*. The fact that chiro-optical response cannot be simply described in terms of one or few excitations justifies and actually calls for the introduction of advanced analysis tools such as ICM and RSD, which provide a synthetic and potentially insightful overview of the main types of contributions at play in the real or momentum space determining chiro-optical phenomena.

4. CONCLUSIONS

We have introduced and exemplified the use of individual component map of rotatory strength (ICM-RS) and rotatory strength density (RSD) plots as analysis tools of TDDFT simulations.

RSD and ICM-RS are two alternative tools to visualize chiro-optical response either in real space or in the conjugate space of molecular orbitals. In particular, ICM-RS analysis follows the lines of and deepens the connection between chiro-optical response and single-particle excitations in the density-matrix form of linear-response self-consistent theory[9,10,20] and at the same time extends it (a) to include chiral activity and (b) to keep track of sign factors due to alignment (coherence, constructive interference) or opposition (destructive interference) of dipole and density-matrix contributions of individual occupied/virtual orbital pairs, i.e., of coherence or interference between perturbation and property. We reported both 3D and 2D ICM-RS$(\omega, x$ or y or $z)$ plots, associated with the density of rotatory strength in the orbital space, and RSD$(\omega, x$ or y or $z)$ plots, associated with the density of rotatory strength in real

space. The ICM-RS analysis corresponds to the analogue for chiro-optical response of the recently introduced individual component map of oscillatory strength (ICM-OS) plots for absorption.[38]

$(Ag-Au)_{30}(SR)_{18}$ monolayer-protected bimetallic nanoclusters were selected as test cases, and their chiro-optical response was shown to present a rich phenomenology which is both representative of the behavior of complex systems and in which the coexistence of chiral and strongly anisotropic behavior is appealing, e.g., for sensing and bioapplications, as it can provide information on anisotropic biomolecules or on systems in typically anisotropic arrangement such as interacting with a surface. Indeed, it can be expected that for applications of these systems in a bioenvironment (e.g., sensing or as markers) all these features, strong absorption, anisotropic, and chiral activity, will simultaneously be crucial in controlling their functionality.

The phenomenology deriving from ICM-RS and RSD analysis in the investigated test cases is complex but can be summarized in terms of three key features.

The first general observation is the ubiquitous presence of long-range off-diagonal terms[16] in all ICM-RS(ω, x or y or z) plots here investigated and their importance in shaping chiro-optical response, producing enhancement or quenching in rotatory strength. This therefore seems to be a distinctive feature of the chiro-optical response of complex systems such as metal nanoclusters or nanoparticles.

Considering that the final goal of an analysis of chiro-optical MPC spectra is to ascertain the origin of response as a function of core/staple structure and ligand chemistry, so as to be able to orient the synthesis of new compounds and achieve a rational design of optimal systems, in the present ICM-RS/RSD analysis particular attention has then been paid to cancellation effects, whose control is crucial to enhance or damp chiro-optical response. Three scenarios have been encountered and outlined above, which can be basically reduced to two, according to whether destructive interference and cancellation in chiro-optical response arise from regions of the $(\varepsilon_i, \varepsilon_a)$ occupied/virtual orbital plane corresponding to similar or dissimilar excitation energies. It has been argued that the latter case (cancellation arising from single-particle excitations exhibiting dissimilar orbital energies) better lends itself to rational design, as it should be more sensitive to the details of Hamiltonian couplings and therefore could be manipulated by substituting different metal elements as here investigated (doping) or by changing the nature of the ligand, e.g., switching from thiolates to selenolates.

It is useful to note in this respect a third key feature of the present analysis, i.e., that linear response in eq 1 can be seen as a scalar product between density-matrix and dipole-matrix elements in the double space of occupied/virtual pairs. This entails that the maximum achievable value of the response is obtained when such vectors are optimally aligned (vice versa, the minimum achievable value is obtained for orthogonal operators), thus providing a mathematical basis for optimal tuning.

In terms of perspectives, a natural development of the present approach is to combine ICM-RS with other analytic tools, such as the projection of TDDFT spectra onto fragments, freely defined as chemical parts of the systems or functional basis sets (e.g., s/p and d bands). This will allow us to exploit the merits of both ICM-RS and previous real-space fragment analysis tools[16−20] including the recently introduced variants of fragment projection developed for MPC systems.[21] This should allow one to disentangle, within the class of response enhancement phenomena, plasmonic vs molecular-like contributions to both absorption[48] and CD, where plasmonics effects can be associated with both traditional plasmons or with "re-birth" phenomena due to matching of orbital levels and resonance conjugation[21,49]), or to single out, within the class of response quenching phenomena, their physical origin, such as d-screening. These perspectives are currently under study in our laboratories.

■ ASSOCIATED CONTENT

● Supporting Information

Pictorial illustration of the $Au_{30}(SCH_3)_{18}$ skeleton, CD spectra distinguished into Cartesian components of the propagation direction, ICM-RS plots for (A) $Au_{30}(SR)_{18}$, (B) $Ag_2Au_{28}(SR)_{18}$, and (C) $Ag_{16}Au_{14}(SR)_{18}$ nanoclusters at selected energy values (1.55, 1.65, and 3.05 eV), ICM-ED[$\mu_{x,y,z}$] and ICM-MD[$m_{x,y,z}$] plots for the $Ag_{16}Au_{14}(SR)_{18}$ nanocluster, and energetics of single Ag doping into the $Au_{30}(SR)_{18}$ nanocluster (PDF)

■ AUTHOR INFORMATION

Corresponding Authors
*E-mail: stener@units.it.
*E-mail: alessandro.fortunelli@cnr.it.

ORCID ⓘ
Daojian Cheng: 0000-0001-7977-0750
Daniele Toffoli: 0000-0002-8225-6119
Edoardo Aprà: 0000-0001-5955-0734
Mauro Stener: 0000-0003-3700-7903
Alessandro Fortunelli: 0000-0001-5337-4450

Author Contributions
#L.C. and O.B. are equally contributing first authors.

Notes
The authors declare no competing financial interest.

■ REFERENCES

(1) Whetten, R. L.; Khoury, J. T.; Alvarez, M. M.; Murthy, S.; Vezmar, I.; Wang, Z. L.; Stephens, P. W.; Cleveland, C. L.; Luedtke, W. D.; Landman, U. Nanocrystal gold molecules. *Adv. Mater.* **1996**, *8*, 428−433.

(2) Jin, R.; Zeng, C.; Zhou, M.; Chen, Y. Atomically precise colloidal metal nanoclusters and nanoparticles: Fundamentals and opportunities. *Chem. Rev.* **2016**, *116*, 10346−10513.

(3) Tsukuda, T.; Häkkinen, H. *Protected metal clusters: From fundamentals to applications*, 1st ed.; Elsevier: 2015; Vol. 9, p 372.

(4) Kumara, C.; Jupally, V. R.; Dass, A. Gold thiolate nanomolecules: Synthesis, mass spectrometry, and characterization. *Struct. Bonding (Berlin, Ger.)* **2014**, *161*, 155−187.

(5) Fernando, A.; Weerawardene, K. L. D. M.; Karimova, N. V.; Aikens, C. M. Quantum Mechanical Studies of Large Metal, Metal Oxide, and Metal Chalcogenide Nanoparticles and Clusters. *Chem. Rev.* **2015**, *115*, 6112−6216.

(6) Antonello, S.; Maran, F. Molecular electrochemistry of monolayer-protected clusters. *Current Opinion Electrochem.* **2017**, *2*, 18−25.

(7) Agrachev, M.; Antonello, S.; Dainese, T.; Ruzzi, M.; Zoleo, A.; Aprà, E.; Govind, N.; Fortunelli, A.; Sementa, L.; Maran, F. Magnetic ordering in gold nanoclusters. *ACS Omega.* **2017**, *2*, 2607−2617.

(8) Barcaro, G.; Sementa, L.; Fortunelli, A.; Stener, M. Optical properties of nanoalloys. *Phys. Chem. Chem. Phys.* **2015**, *17*, 27952−27967.

(9) McWeeny, R. *Methods of molecular quantum mechanics, Academic Press*, 2nd ed.; Elsevier: London, 1989.

(10) Malola, S.; Lehtovaara, L.; Enkovaara, J.; Häkkinen, H. Birth of the localized surface plasmon resonance in monolayer-protected gold nanoclusters. *ACS Nano* **2013**, *7*, 10263−10270.

(11) Savarese, M.; Guido, C. A.; Brémond, E.; Ciofini, I.; Adamo, C. Metrics for molecular electronic excitations: A comparison between orbital- and density-based descriptors. *J. Phys. Chem. A* **2017**, *121*, 7543−7549.

(12) Crawford, T. D. Ab initio calculation of molecular chiroptical properties. *Theor. Chem. Acc.* **2006**, *115*, 227−245.

(13) Noguez, C.; Garzon, I. L. Optically active metal nanoparticles. *Chem. Soc. Rev.* **2009**, *38*, 757−771.

(14) Knoppe, S.; Bürgi, T. Chirality in thiolate-protected gold clusters. *Acc. Chem. Res.* **2014**, *47*, 1318−1326.

(15) Sarem, M.; Lüdeke, S.; Thomann, R.; Salavei, P.; Zou, Z.; Habraken, W.; Masic, A.; Shastri, V. P. Disordered conformation with low PII helix in phosphoproteins orchestrates biomimetic apatite formation. *Adv. Mater.* **2017**, *29*, 1701629.

(16) Murphy, V. L.; Kahr, B. Hückel Theory and Optical Activity. *J. Am. Chem. Soc.* **2015**, *137*, 5177−5183.

(17) Moore, B., II; Srebro, M.; Autschbach, J. Analysis of Optical Activity in Terms of Bonds and Lone-Pairs: The Exceptionally Large Optical Rotation of Norbornenone. *J. Chem. Theory Comput.* **2012**, *8*, 4336−4346.

(18) Yao, H. Chiral ligand-protected gold nanoclusters: Considering the optical activity from a viewpoint of ligand dissymmetric field. *Prog. Nat. Sci.* **2016**, *26*, 428−439.

(19) Caricato, M.; Vaccaro, P. H.; Crawford, T. D.; Wiberg, K. B.; Lahiri, P. Insights on the Origin of the Unusually Large Specific Rotation of (1S,4S)-Norbornenone. *J. Phys. Chem. A* **2014**, *118*, 4863−4871.

(20) Caricato, M. Orbital Analysis of Molecular Optical Activity Based on Configuration Rotatory Strength. *J. Chem. Theory Comput.* **2015**, *11*, 1349−1353.

(21) Sementa, L.; Barcaro, G.; Baseggio, O.; Vetta, M. D.; Dass, A.; Aprà, E.; Stener, M.; Fortunelli, A. Ligand-enhanced optical response of gold nanomolecules and its fragment projection analysis: The case of $Au_{30}(SR)_{18}$. *J. Phys. Chem. C* **2017**, *121*, 10832−10842.

(22) Hutter, J.; Iannuzzi, M.; Schiffmann, F.; VandeVondele, J. CP2K: Atomistic simulations of condensed matter systems. *WIREs: Comput. Mol. Sci.* **2014**, *4*, 15−25.

(23) Lippert, G.; Hutter, J.; Parrinello, M. The Gaussian and augmented-plane-wave density functional method for ab initio molecular dynamics simulations. *Theor. Chem. Acc.* **1999**, *103*, 124−140.

(24) Goedecker, S.; Teter, M.; Hutter, J. Separable dual-space Gaussian pseupotentials. *Phys. Rev. B: Condens. Matter Mater. Phys.* **1996**, *54*, 1703−1710.

(25) VandeVondele, J.; Hutter, J. Gaussian basis sets for accurate calculations on molecular systems in gas and condensed phases. *J. Chem. Phys.* **2007**, *127*, 114105.

(26) Grimme, S.; Antony, J.; Ehrlich, S.; Krieg, H. A consistent and accurate ab initio parametrization of density functional dispersion correction (DFT-D) for the 94 elements H-Pu. *J. Chem. Phys.* **2010**, *132*, 154104.

(27) Perdew, J. P.; Burke, K.; Ernzerhof, M. Generalized gradient approximation made simple. *Phys. Rev. Lett.* **1996**, *77*, 3865−3868.

(28) Dass, A.; Jones, T.; Rambukwella, M.; Crasto, D.; Gagnon, K. J.; Sementa, L.; Vetta, M. D.; Baseggio, O.; Aprà, E.; Stener, M.; Fortunelli, A. Crystal structure and theoretical analysis of green gold $Au_{30}(S\text{-}tBu)_{18}$ nanomolecules and their relation to $Au_{30}S(S\text{-}tBu)_{18}$. *J. Phys. Chem. C* **2016**, *120*, 6256−6261.

(29) Baerends, E. J.; Ellis, D. E.; Ros, P. Self-consistent molecular Hartree-Fock-Slater calculations I. The computational procedure. *Chem. Phys.* **1973**, *2*, 41−51.

(30) Baseggio, O.; Fronzoni, G.; Stener, M. A new time dependent density functional algorithm for large systems and plasmons in metal clusters. *J. Chem. Phys.* **2015**, *143*, 024106.

(31) Baseggio, O.; Vetta, M. D.; Fronzoni, G.; Stener, M.; Fortunelli, A. A new time-dependent density-functional method for molecular plasmonics: Formalism, implementation, and the $Au_{144}(SH)_{60}$ case study. *Int. J. Quantum Chem.* **2016**, *116*, 1603−1611.

(32) Baseggio, O.; Vetta, M. D.; Fronzoni, G.; Stener, M.; Sementa, L.; Fortunelli, A.; Calzolari, A. Photoabsorption of icosahedral noble metal clusters: An efficient TDDFT approach to large-scale systems. *J. Phys. Chem. C* **2016**, *120*, 12773−12782.

(33) Baseggio, O.; Toffoli, D.; Fronzoni, G.; Stener, M.; Sementa, L.; Fortunelli, A. Extension of the time-dependent density functional complex polarizability algorithm to circular dichroism: Implementation and applications to Ag_8 and $Au_{38}(SC_2H_4C_6H_5)_{24}$. *J. Phys. Chem. C* **2016**, *120*, 24335−24345.

(34) van Leeuwen, R.; Baerends, E. J. Exchange-correlation potential with correct asymptotic behavior. *Phys. Rev. A: At., Mol., Opt. Phys.* **1994**, *49*, 2421−2431.

(35) Gross, E. K. U.; Kohn, W. Time-dependent density-functional theory. *Adv. Quantum Chem.* **1990**, *21*, 255−291.

(36) Lenthe, E. v.; Baerends, E. J.; Snijders, J. G. Relativistic regular two-component Hamiltonians. *J. Chem. Phys.* **1993**, *99*, 4597−4610.

(37) Autschbach, J.; Ziegler, T.; van Gisbergen, S. J. A.; Baerends, E. J. Chiroptical Properties from Time-Dependent Density Functional Theory. I. Circular Dichroism Spectra of Organic Molecules. *J. Chem. Phys.* **2002**, *116*, 6930−6940.

(38) Theivendran, S.; Chang, L.; Mukherjee, A.; Sementa, L.; Stener, M.; Fortunelli, A.; Dass, A. Principles of optical spectroscopy of aromatic alloy nanomolecules: $Au_{36-x}Ag_x(SPhtBu)_{24}$. *J. Phys. Chem. C* **2018**, *122*, 4524−4531.

(39) Crasto, D.; Dass, A. Green gold: $Au_{30}(S\text{-}t\text{-}C_4H_9)_{18}$ molecules. *J. Phys. Chem. C* **2013**, *117*, 22094−22097.

(40) Higaki, T.; Liu, C.; Zeng, C.; Jin, R.; Chen, Y.; Rosi, N. L.; Jin, R. Controlling the atomic structure of Au_{30} nanoclusters by a ligand-based strategy. *Angew. Chem., Int. Ed.* **2016**, *55*, 6694−6697.

(41) Fortunelli, A.; Sementa, L.; Thanthirige, V. D.; Jones, T. C.; Stener, M.; Gagnon, K. J.; Dass, A.; Ramakrishna, G. $Au_{21}S(SAdm)_{15}$: An anisotropic gold nanomolecule. Optical and photoluminescence spectroscopy and first-principles theoretical analysis. *J. Phys. Chem. Lett.* **2017**, *8*, 457−462.

(42) Khandelwal, P.; Poddar, P. Fluorescent metal quantum clusters: an updated overview of the synthesis, properties, and biological applications. *J. Mater. Chem. B* **2017**, *5*, 9055−9084.

(43) Juarez-Mosqueda, R.; Malola, S.; Hakkinen, H. Stability, electronic structure, and optical properties of protected gold-doped silver $Ag_{29-x}Au_x$ (x = 0−5) nanoclusters. *Phys. Chem. Chem. Phys.* **2017**, *19*, 13868−13874.

(44) Cantelli, A.; Guidetti, G.; Manzi, J.; Caponetti, V.; Montalti, M. Towards ultra-bright gold nanoclusters. *Eur. J. Inorg. Chem.* **2017**, *2017*, 5068−5084.

(45) Almansaf, A. A.; Parida, M. R.; Besong, T. M. D.; Maity, P.; Bootharaju, M. S.; Bakr, O. M.; Mohammed, O. F. The impact of Au doping on the charge carrier dynamics at the interfaces between

cationic porphyrin and silver nanoclusters. *Chem. Phys. Lett.* **2017**, *683*, 393−397.

(46) Zhang, B.; Bürgi, T. Doping silver increases the $Au_{38}(SR)_{24}$ cluster surface flexibility. *J. Phys. Chem. C* **2016**, *120*, 4660−4666 ù.

(47) Rambukwella, M.; Chang, L.; Ravishanker, A.; Fortunelli, A.; Stener, M.; Dass, A. Au36(SePh)24 nanomolecules: synthesis, optical spectroscopy and theoretical analysis. *Phys. Chem. Chem. Phys.* **2018**, *20*, 13255−13262.

(48) Zhang, R.; Bursi, L.; Cox, J. D.; Cui, Y.; Krauter, C. M.; Alabastri, A.; Manjavacas, A.; Calzolari, A.; Corni, S.; Molinari, E.; Carter, E. A.; Garcia de Abajo, F. J.; Zhang, H.; Nordlander, P. How to identify plasmons from the optical response of nanostructures. *ACS Nano* **2017**, *11*, 7321−7335.

(49) Sementa, L.; Barcaro, G.; Dass, A.; Stener, M.; Fortunelli, A. Designing ligand-enhanced optical absorption of thiolated gold nanoclusters. *Chem. Commun.* **2015**, *51*, 7935−7938.